Kim et al. *NPG Asia Materials* (2024) 16:23
https://doi.org/10.1038/s41427-024-00543-x

NPG Asia Materials

ARTICLE Open Access

Investigation on mussel periostracum, a viscoelastic-to-poro-gel graded material, as an interface between soft tissue and rigid materials

Hyungbin Kim[1,2], Heejin Lim[3], Sangsik Kim[4], Jun Mo Koo[5], Chanoong Lim[6], Hojung Kwak[7], Dongyeop X. Oh[8] and Dong Soo Hwang[1,2,9]

Abstract

Mussel periostracum, a nonliving multifunctional gel that covers the rigid inorganic shells of mussels, provides protection against mechanical impacts, biofouling, and corrosion in harsh ocean environments. The inner part of the periostracum, which emerges from biological tissues, functions as a natural interface between tissue and inorganic materials. The periostracum shows significant potential for application in implantable devices that provide interfaces; however, this system remains unexplored. In this study, we revealed that the inner periostracum performs graded mechanical functions and efficiently dissipates energy to accommodate differences in stiffness and stress types on both sides. On the tissue end, the lightly pigmented periostracum exhibits extensibility and energy dissipation under repetitive tension. This process was facilitated by the slipping and reassembly of β-strands in the discovered major proteins, which we named periostracin proteins. On the shell end, the highly pigmented, mineralized, and porous segment of the periostracum provided stiffness and cushioned against compressive stresses exerted by the shell valves during closure. These findings offer a novel possibilities for the design of interfaces that bridge human tissue and devices.

Introduction

Significant advancements have been made in the development of hydrogels for medical applications. Specifically, functional hydrogels have emerged as promising materials that can provide effective interfaces between the human body and implantable devices, as hydrogels mechanically and chemically resemble biological tissues[1]. However, despite considerable efforts in establishing hydrogel interfaces, maintaining long-term functionality at dissimilar interfaces is difficult, as multiple stresses must be addressed simultaneously. There are remarkable examples of material interfaces in the natural world. For example, cartilage, which has low stiffness yet high durability, efficiently dissipates compressive loads between bones[2]. Through a stiffness gradient, mussel byssus seamlessly bridges hard rock surfaces with soft secretory tissue, preventing mechanical failure during tensile loading[3]. Interestingly, this study highlights the potential of the inner periostracum in mussels as a more suitable example for connecting soft biological tissue with rigid, nonliving inorganic materials.

Mussels, as sessile organisms, thrive in highly dynamic ocean environments by developing strong and durable mineralized shells to protect their internal soft bodies[4]. While the shell primarily consists of three layers (nacre, prism, and periostracum), the nacreous and prismatic layers are predominantly composed of minerals. In contrast, the periostracum, an inconspicuous layer, is primarily composed of tanned proteins with detectable mineralized inclusions[5]. The periostracum comprises the

Correspondence: Dongyeop X. Oh (d.oh@inha.ac.kr) or Dong Soo Hwang (dshwang@postech.ac.kr)
[1]Division of Environmental Science and Engineering, Pohang University of Science and Technology (POSTECH), Pohang 37673, Republic of Korea
[2]School of Interdisciplinary Bioscience and Bioengineering, Pohang University of Science and Technology (POSTECH), Pohang 37673, Republic of Korea
Full list of author information is available at the end of the article

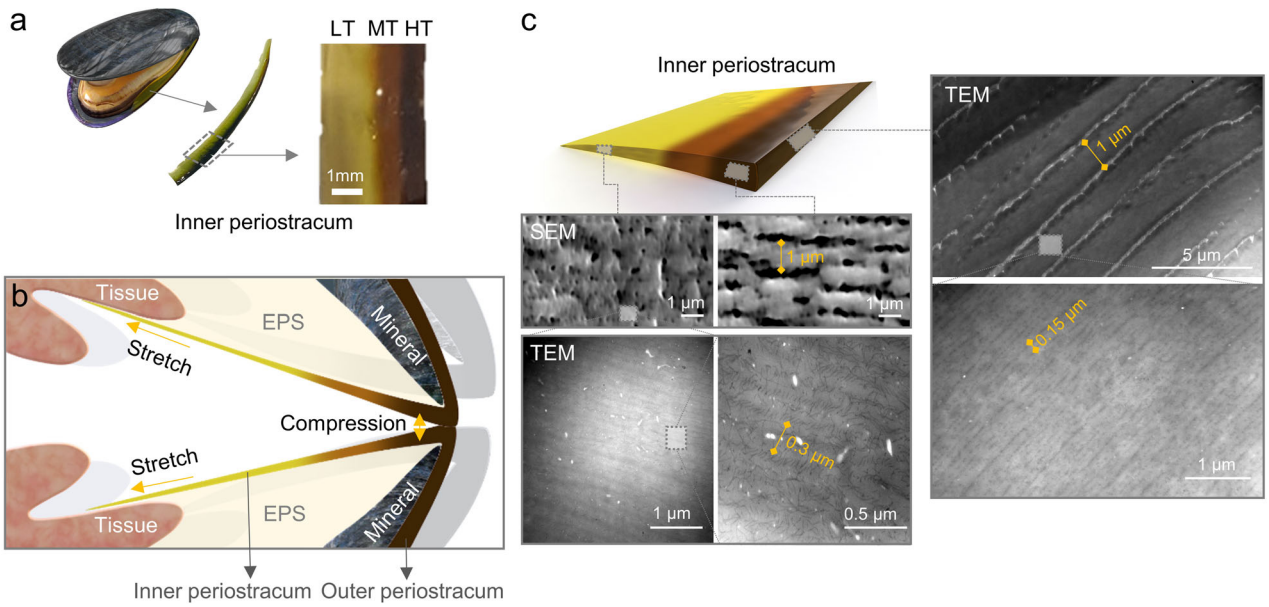

Fig. 1 Graded assembly of the inner periostracum. a Photographs of the harvested inner periostracum. **b** Illustration of the inner periostracum that experienced spatially distinct stresses. **c** Observations of the inner periostracum through an electron microscope.

following distinct parts (see Fig. 1): the outer periostracum, which is attached to the surface of the prismatic layer, and the inner periostracum, which connects the tissue to the edge of the shell. The inner periostracum undergoes a maturation process, gradually transforming into a graded material from the tissue to the end of the shell through pigmentation and thickening. Eventually, the fungus becomes integrated into the shell to form the outer periostracum. The outer periostracum exhibits protective functions, such as wear resistance and antifouling, contributing to the safeguarding of the mineral phase[6,7]. Conversely, the inner periostracum may act as a barrier, isolating the biomineralization process occurring in the extrapallial space (EPS) from seawater. Additionally, the inner periostracum functions as a scaffold in which mineral crystals generated in the EPS are deposited[8,9].

To consistently fulfill the aforementioned biological roles, the inner periostracum appears to possess excellent durability with adaptive material properties, addressing the following mechanical challenges: 1) stiffness mismatch and 2) energy dissipation for spatially diverse types of stress. First, the inner periostracum tackles mechanical issues arising from the stiffness mismatch between the mineral phase (~ 40 GPa) and the tissue phase (< 1 MPa). The cross-linking of DOPA (3,4-dihydroxyphenylalanine), a post-translationally modified amino acid found in some biological materials, is closely associated with an increase in stiffness. An illustrative example is the beak of a squid, in which stiffness significantly increases due to the crosslinking of DOPA to precursor proteins through a tanning reaction[10]. Given that the inner periostracum exhibits graded pigmentation, as shown in Fig. 1a, this crosslinking may be used to establish stiffness gradients that link mechanically dissimilar tissues. Second, the inner periostracum must optimally withstand different mechanical loads at each end (see Fig. 1b). For instance, the area around the tissue undergoes repetitive stretching and shearing due to tissue contraction/relaxation movements, while the portion at the shell's edge experiences strong compressive loads as the shell tightly closes under the force of the adductor muscle to completely enclose internal tissues. Mussel shells and claws exhibit comparable closure strength when their lengths are similar[11]. Therefore, the inner periostracum, which exhibits adaptive properties to effectively handle spatially diverse stress types, may offer novel insights for developing energy-absorbing materials for soft-hard interfaces. In particular, in engineered hydrogels, increasing stiffness through covalent crosslinking often results in a decrease in energy dissipation capacity[12]. Investigating how the inner periostracum minimizes this inverse relationship would be intriguing. However, the structure-property relationships of these systems are poorly understood.

This study explored the structure–property relationships of graded regions within the inner periostracum. The investigation revealed that the inner periostracum undergoes a transition in stiffness through mineralization and cross-linking between the soft tissue and hard inorganic material. Surprisingly, the inner periostracum demonstrated an efficient capability of energy dissipation and was suitable for applied stresses in all regions,

irrespective of the stiffness level. In the tissue region, a nonporous composition prevailed and was characterized by a semicrystalline fibrous network of periostracin, consisting of β-sheets and disordered secondary structures. When subjected to tension, energy dissipation occurred through the slippage of weakened β-strand chains, which was facilitated by the formation of hydrogen bonds with water molecules. On the shell side, a porous structure with unidirectional aligned channels was observed. Compression resulted in the expulsion of water within the channels, leading to stress relaxation. These findings on graded structured materials, which involve combining efficient energy dissipation and a stiffness gradient, may inspire the development of next-generation biointerfaces within the human body.

Results

Observation of hierarchical structure

The hierarchical organization of the inner periostracum was investigated through electron microscopic observations. The electron microscopy images depict porous structure and protein fibrils in a thin section of the inner periostracum (see Fig. 1c). Scanning electron microscopy (SEM) images reveal noncircular micropores in transverse sections. In the longitudinal section of the transmission electron microscopy (TEM) image, these pores formed by unidirectionally aligned channels at a constant spacing of ~1 μm along the shell edge, consistent with the intervals observed in the SEM image. Previous research has indicated that a fully matured periostracum attached to the mineral phase has open pores, which function as water reservoirs that can be squeezed out[7]. Consequently, these aligned channels serve as water pores to alleviate mechanical stress. Given that the pore size gradually increases on the shell side compared to the tissue side, these channels are more actively utilized on the shell side. On the nanoscale, the transverse TEM sections revealed a horizontally aligned fibrillar texture, forming a regular pattern of stacked layers with an interlayer spacing of ~100–300 nm. Upon closer observation, the central region of the layer appeared denser and more packed than the surrounding area. This structure resembles a network of brush polymer materials with amorphous chains that surround the crystalline core. Amorphous or brush polymers with free chains are frequently employed to confer conventional viscoelasticity to hydrogels and elastomers, as chain relaxation results in energy dissipation[13]. Thus, the hierarchical assembly from water channels to a semicrystalline structure is highly relevant to the viscoelastic behavior of this material.

Identification and characterization of building block proteins

In a previous study, a constituent precursor protein named periostracin was obtained from the periostracum and was partially purified[14]. This protein is rich in Gly (55%) and Tyr (10%), similar to the amino acid composition of the entire periostracum (Table S1); however, the amino acid sequence of periostracum has not been previously determined. To map the distribution of Tyr and Gly secondary ions, ToF-SIMS was employed based on the spectral features of the amino acids[15]. The resulting images illustrated that these ions are evenly distributed throughout the samples (see Fig. S1), suggesting that Gly–Tyr-rich proteins are the predominant precursor proteins. Therefore, in this work, we attempted to identify Gly–Tyr-rich proteins.

We characterized several Gly–Tyr-rich proteins derived from the periostracum through protein sequencing via LC–MS/MS guided by the transcriptome. The transcriptome was generated from mantle tissue cells, and mass spectra were obtained from extracted peptides through direct digestion by trypsin. Consequently, full sequences of three Gly–Tyr-rich proteins, namely, periostracin-1, -2, and -3, were obtained (see Fig. S2 and Table S2). These proteins are distinct from mineralization-related matrix proteins that are produced in the same marginal mantle cells, as the proteins contain more negatively charged amino acids than periostracins (see Table S3)[16]. The newly discovered periostracins share several characteristics, such as a high Gly-Tyr-rich composition, low complexity, and similar secondary structures (see Fig. 2). These strains contained high levels of Gly (above 36.8%) and Tyr (above 7.6%), similar to the amino acid composition of the bulk periostracum (54% Gly and 13–16% Tyr). The periostracin proteins feature Gly/Gly-Tyr-rich regions (e.g., the GGY motif) lacking charged amino acids at the C- and/or N-termini. Secondary structure analysis using I-TASSER and AlphaFold predicted that Gly-Tyr-rich regions are intrinsically disordered regions (IDRs) with low complexity, while the remaining middle regions are predicted to be ordered β-sheets. The predicted assembly suggested that the protein is primarily composed of the IDR, with a small proportion of β-sheets. This structure aligns with the random structure of individual fibers observed via TEM, in which β-sheet structures could not be assigned (see Fig. 1c). Moreover, FT-IR, widely used for protein secondary structure analysis, showed an intense peak at 1632 cm^{-1} corresponding to β-sheets (see Fig. S3). Additionally, these proteins have high isoelectric points (pIs > 9), and their Gly–Tyr-rich motifs tend to be hydrophobic according to hydropathy analyses. These molecular features endow the periostracins with H-bond hydropathy, consistent with the reversible water extrusion inside the protein network upon external load application.

Gradients in biochemical compositions

Figure 1a shows a pigmentation gradient from the tissue side (yellow) to the shell side (black) of the inner

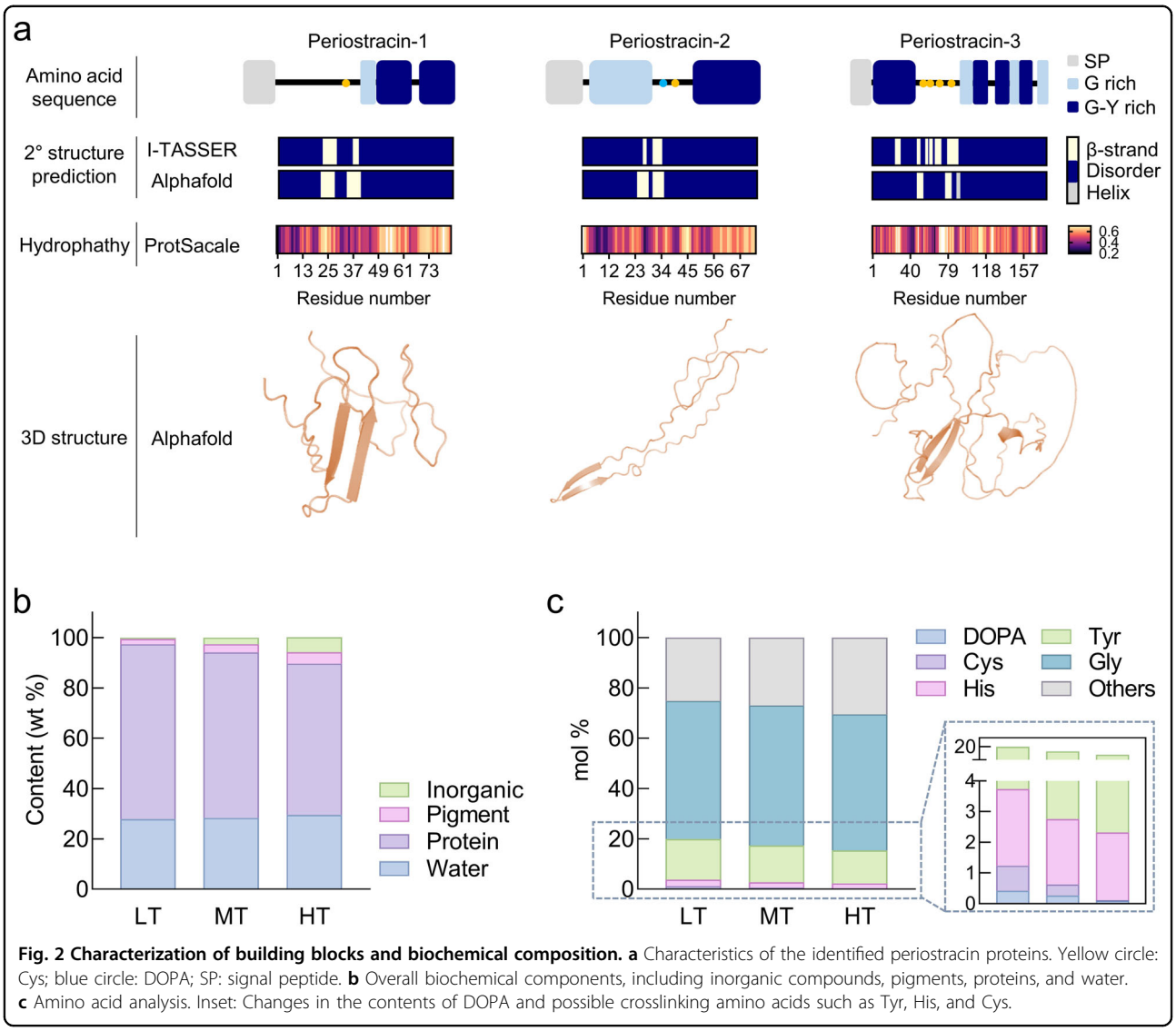

Fig. 2 Characterization of building blocks and biochemical composition. a Characteristics of the identified periostracin proteins. Yellow circle: Cys; blue circle: DOPA; SP: signal peptide. **b** Overall biochemical components, including inorganic compounds, pigments, proteins, and water. **c** Amino acid analysis. Inset: Changes in the contents of DOPA and possible crosslinking amino acids such as Tyr, His, and Cys.

periostracum, imparting distinct material properties on both sides. To explore the gradient in biochemical properties, the inner periostracum was divided into the following parts based on visible pigmentation: lightly tanned (LT), moderately tanned (MT), and heavily tanned (HT).

The biochemical composition of each cut-out was subsequently investigated through gravimetric analyses. A previous study suggested that the periostracum primarily consists of protein, minerals, and pigments[10]. As shown in Fig. 2b, the overall gradient of biochemical compositions is evident. LTs are exclusively composed of proteins. In contrast, compared to LT and MT, HT exhibited significantly greater pigment and mineral contents (6 and 9 wt%, respectively), resulting in a greater elastic modulus. Surprisingly, the water content of all the portions was similar, measuring 23 wt%. This result is unusual, as hydrophobic pigments typically repel water molecules from the protein network[10]. It is inferred that the hydrogel-like LT is relatively hydrophilic and adsorbs water molecules in the protein matrix, while porous HT is relatively hydrophobic and absorbs water through its aligned porous channels[17]. Moreover, compared with the LT part, the HT part demonstrates dehydration resistance because its channels maintain hydration (see Fig. S4). HTs at the shell end are often exposed to sunlight/air during low tide, whereas LTs remain hydrated by body fluids. Hence, this graded porosity is likely an adaptive architecture that caters to specific functional demands.

Crosslinking chemistry is crucial in unraveling the fabrication processing of robust materials[18]. In the cutouts of the inner periostracum, certain amino acids gradually decreased, such as Cys, His, and Tyr, which readily react with DOPA to form crosslinks (see Fig. 2c). These findings suggest that these amino acids were involved in the

process of sclerotization. Crosslinks of DOPA-His (351 m/z), DOPA-Cys (317 m/z), and DOPA-Tyr (377 m/z) were found through fragmentation analysis of MS2 spectra from LC–MS/MS (see Fig. S5). Specifically, the concentrations of DOPA and Cys significantly decreased to zero from LT to HT, implying that cysteinyl DOPA is related to the pigmentation process and that pigmentation and crosslinking are intertwined. The relationship between Cys and DOPA is well established in melanogenesis chemistry[19]. According to the transcriptome-guided mass analysis of periostracal proteins, five Cys-rich proteins (14–23%) with low molecular weights were identified alongside periostracin (Table S2). These periostracal Cys-rich proteins may function as crosslinkers.

Different mechanical adaptations of the inner periostracum

The function of biological materials is closely linked to the biomolecules they contain. The aforementioned composition gradient may influence the spatially diverse mechanical functions of the inner periostracum. To explore this phenomenon, we conducted tensile and compressive tests on the cut samples from LT to HT to evaluate their mechanical effects (see Fig. 3). According to the tensile results (Fig. 3a, b), the LT sample exhibited extensibility up to 100% strain with a stiffness of 11.5 MPa, while the HT sample exhibited extension to 25% strain with high stiffness at 44.3 MPa. This stiffness gradient may result from mineralization and pigmentation. However, the tensile strength decreased from 9.57 MPa for LT to 5.05 MPa for HT. This unusual strength and stiffness inverse relationship suggests that the LT is highly extensible and robust, while the HT is mechanically unstable under stretching. In contrast, the compressive tests (Fig. 3c, d) demonstrated that HT is well adapted to withstand compressive stress. Under compression, the strength when the sample was compressed to 50% strain gradually increased from 6.46 MPa for LT to 20.17 MPa for HT. These results highlight the distinct mechanical adaptations of LT and HT; LT is highly effective at coping with tissue contraction/relaxation, while HT is robustly compressed to endure shell compression.

Efficient energy dissipation capacity under water

Despite the generation of hydrophobic pigments, the absence of a significant difference in water content, as revealed by the composition results, suggested that water plays a crucial role in determining the mechanical properties of the materials. Given the substantial influence of adequate hydration on adaptive mechanical properties in other biological materials[20,21], it is reasonable to predict that water is an essential element for energy dissipation. Therefore, we investigated the energy dissipation response under repetitive cyclic loading. For the LT samples, the dried specimens were too brittle for testing. However, the hydrated sample exhibited viscoelastic behavior and the initial strain was fully recovered following deformation, indicating high energy dissipation under tension (see Fig. 4a, b). Specifically, the hydrated samples were repetitively cycled three times to 30% strain. During the first cycle, 70% of the tensile stress dissipated, and the strain deformed and partially recovered to 17% due to partial drying during testing at 22 °C and 30% RH. After the second and third cycles, 45–50% of the tensile stress dissipated, and the strain deformation slightly increased. However, the strain fully recovered after 5 min of rehydration. This finding suggested that water hydration in the matrix is critical for realizing reversible elasticity. After rehydration, the tensile cycling of the same sample showed an identical level of energy dissipation as that of plastic deformation. This result implies that the compliant, extensible, and strongly viscous properties of this material are well adapted for mitigating continuous stretching caused by tissue contraction/relaxation in the fully hydrated state. Additionally, we conducted cyclic compressive testing at 30% strain for HT under water (see Fig. 4c, d). The results showed that the hydrated sample repeatedly dissipated compressive stress to ~30% during nine cycles, which was not achieved with the dried sample. This outcome indicates that this portion can repeatedly mitigate the high forces of shell compression by dissipating stress.

Mechanisms of mechanical properties

Understanding the structure–property relationships of naturally occurring materials is crucial for translating the materials into synthetic designs. In our investigation, the hierarchical characteristics revealed the mechanical functions of the inner periostracum. Based on the biochemical results, the inner periostracum is composed of proteins, pigments, and minerals, and the constituent proteins contain ordered β-sheets and disordered regions, particularly originating from the low complexity of Gly–Tyr-rich motifs. Thus, we investigated how these molecular and structural features affect viscoelasticity.

FT-IR-based structural analysis, which is effective for investigating the viscoelastic mechanisms of protein elastomers[22,23], led us to analyze the viscoelastic mechanism of the periostracum based on chemical modification and applied strains using FT-IR analysis. LT was chemically modified using the following treatments: sodium periodate (NaIO4), Ru(II)bpy3/APS, and urea. NaIO4 converts DOPA to DOPAquinone, which subsequently reacts covalently with amino acids such as His, Cys, and Lys. Ru(II)bpy3/APS forms dityrosine residues from nearby tyrosyl free radicals within largely disordered

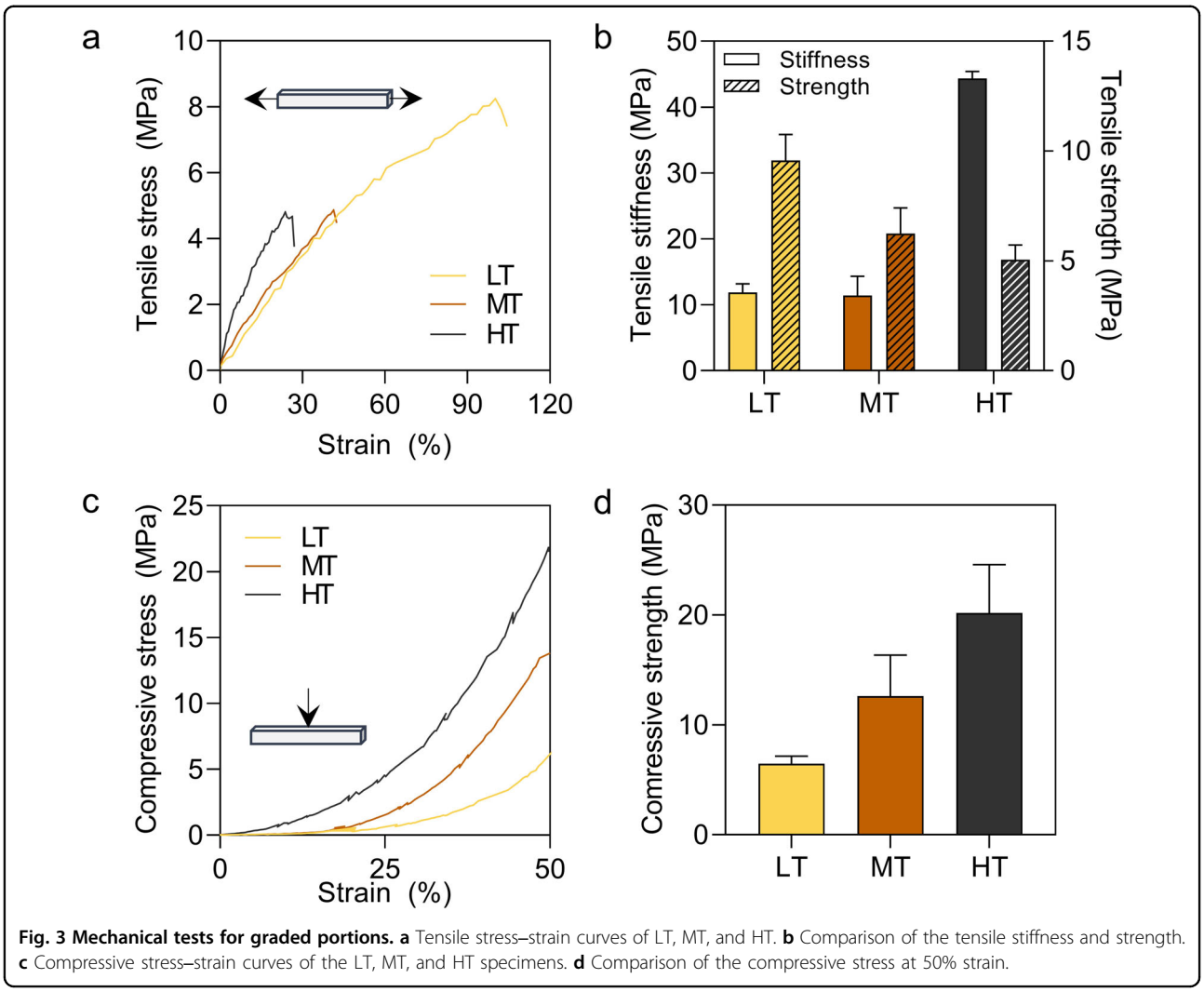

Fig. 3 Mechanical tests for graded portions. a Tensile stress–strain curves of LT, MT, and HT. **b** Comparison of the tensile stiffness and strength. **c** Compressive stress–strain curves of the LT, MT, and HT specimens. **d** Comparison of the compressive stress at 50% strain.

Gly–Tyr-rich regions. 6 M urea, a chaotropic agent, destabilizes β-sheet structures. After urea treatment, the amide I peak shifted from 1632 cm^{-1} to 1619 cm^{-1} (see Fig. 5a). The 1619 cm^{-1} peak could be interpreted as either the formation of Tyr or an intermolecular β-sheet[24,25]. Moreover, the peak at approximately 1700 cm^{-1} and 1515 cm^{-1} decreased in intensity. In a previous study, the intensity of these two peaks increased as β-sheets formed[26]. Considering that urea is a chaotropic agent and that the two peaks decreased, the shift from 1632 cm^{-1} to 1619 cm^{-1} resulted from destabilization of the β-sheet. As apparent in the tensile test results (see Fig. 5b, c), these reagents changed the mechanical properties of LT. Treatment with Ru(II)bpy3/APS, which results in crosslinking and rigidity of the IDR chains, reduced elongation by 0.63 times regardless of stiffness, indicating that the IDR contributes to extensibility under tensile stress. Conversely, it appears that the β-sheet structure contributes to energy dissipation since the urea-treated samples in which the β-sheets were removed appeared to be resilient. Additionally, alkaline peroxidation increased the stiffness by 2.25-fold, explaining why the oxidation of DOPA residues is inhibited during LT for extensibility. Therefore, considering these results collectively, energy dissipation in materials rich in IDRs and β-strands occurs through the slip motion of weakened β-strands, which results from the number of hydrogen bonds formed by the interaction between proteins and water. The flexibility of the IDR also contributes to the extensibility of the material.

HT-containing pigments and minerals were treated with Ru(II)bpy3/APS, alkaline peroxide (H_2O_2), ethylene diamine tetraacetic acid (EDTA), and urea. The pigments were extensively degraded by alkaline H_2O_2 treatment. EDTA is a well-known reagent that is applied to remove minerals from organic matrices. In biological materials mechanically reinforced by metal–ligand coordination[27–29], mechanical reinforcement by inorganic

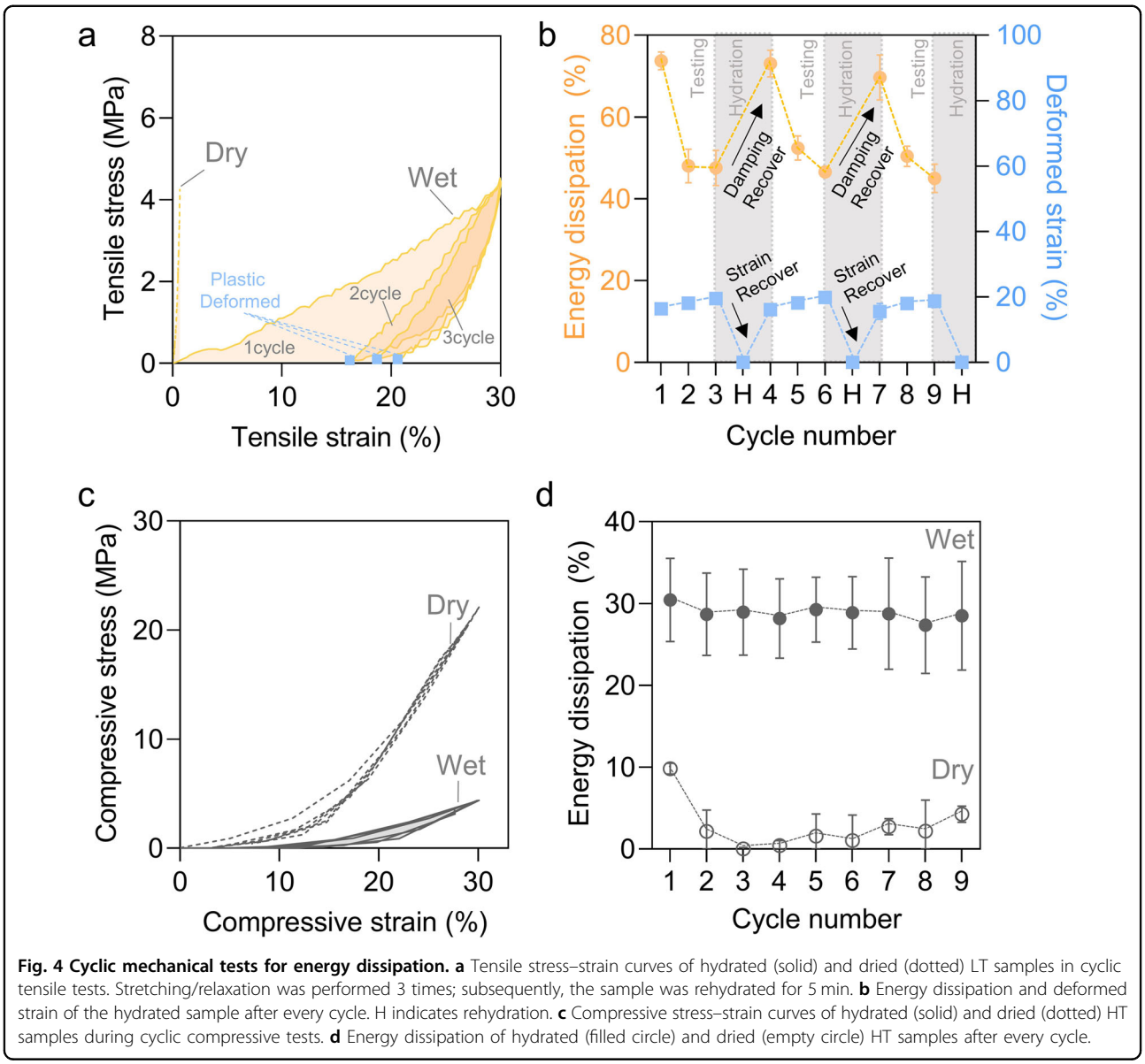

Fig. 4 Cyclic mechanical tests for energy dissipation. a Tensile stress–strain curves of hydrated (solid) and dried (dotted) LT samples in cyclic tensile tests. Stretching/relaxation was performed 3 times; subsequently, the sample was rehydrated for 5 min. **b** Energy dissipation and deformed strain of the hydrated sample after every cycle. H indicates rehydration. **c** Compressive stress–strain curves of hydrated (solid) and dried (dotted) HT samples during cyclic compressive tests. **d** Energy dissipation of hydrated (filled circle) and dried (empty circle) HT samples after every cycle.

additives has been tested by removing the additives using EDTA[30,31]. In many biological materials, disrupting metal–ligand coordination bonds via EDTA typically leads to a reduction in stiffness and toughness. However, in the case of periostracum HTs, compressive stiffness is reduced but the energy dissipation remains unaffected. This distinctive property is a noteworthy characteristic of periostracum HT. Ru(II)bpy3/APS and urea treatments of HT were performed as described for LT. Urea shifted the amide I peak from 1631.8 cm^{-1} to 1619.3 cm^{-1}, indicating a decrease in the amount of β-sheets. A peak shift of 1534.0 cm^{-1} to 1551.9 cm^{-1} was observed for amide II after H_2O_2 treatment. In the silk study, a similar peak shift occurred after heating and was interpreted as the transition from a β-sheet to an α-helix[23]. However, in this system, this shift more likely results from damage to the protein backbone by alkaline conditions. (Fig. 5d). To investigate the mechanical effects of these modifications, we performed a stress relaxation test, which may resembles mussel shell closure (Fig. 5e, f). The tests were conducted by measuring the reduction stress over time after compression to 50% strain. As a result, the structural damage by H_2O_2 and the loss of urea from the β-sheets increased the relaxation by 1.2 and 1.5 times, respectively. In contrast, the reduced flexibility of the IDR chains by dityrosine crosslinking decreased the amount of relaxed stress. This result suggested that the IDR is responsible for stress relaxation through chain reorganization during stress loading. Conversely, demineralization and depigmentation contribute to a decrease in strength, indicating

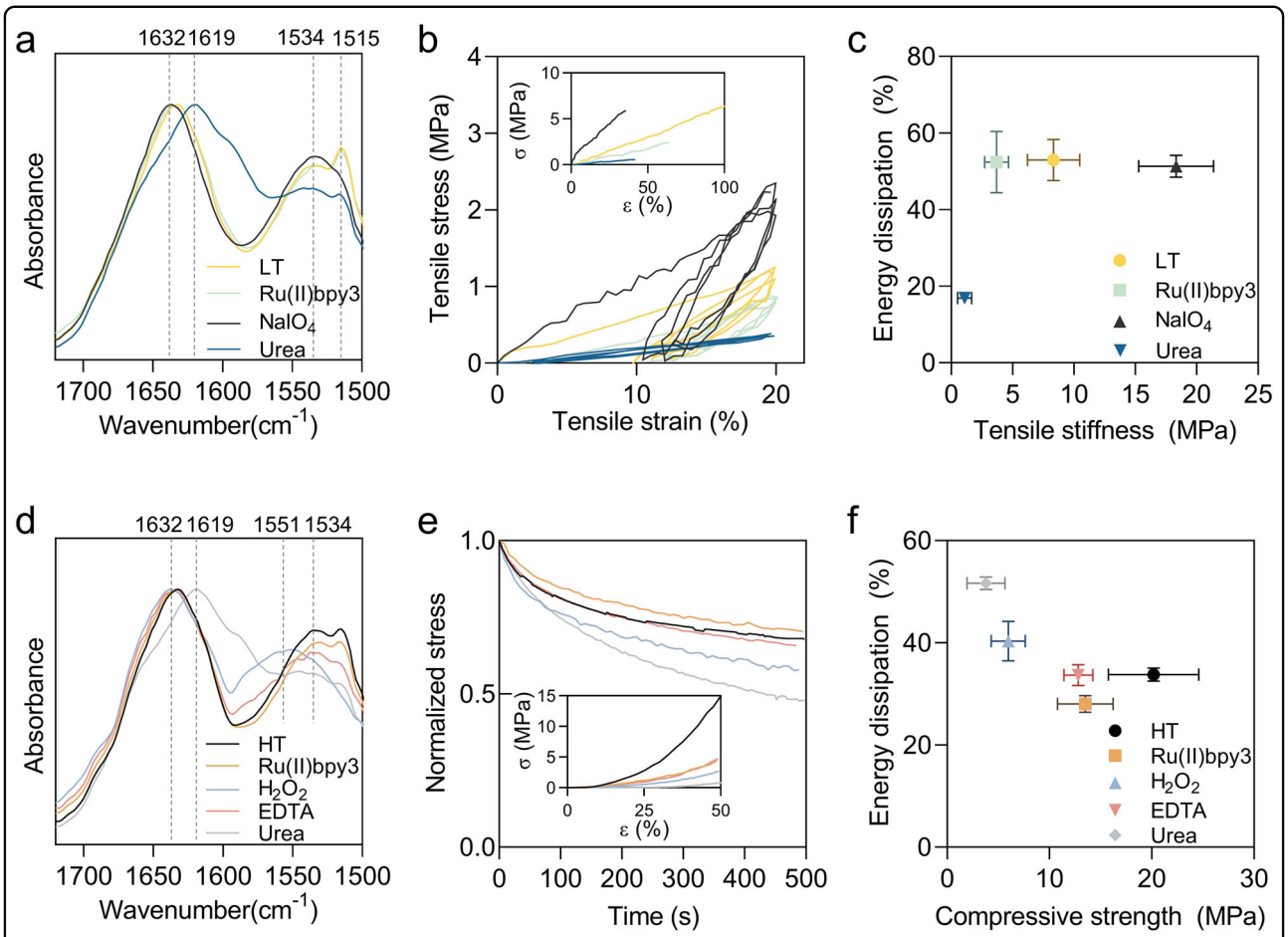

Fig. 5 Molecular mechanisms underlying the mechanical properties. a Secondary structure analysis of LT according to the specific reagents used. **b** Cyclic tensile stress–strain curves of hydrated LTs. Tensile rate: 5 mm/min. Inset: tensile tests. **c** Stiffness–energy dissipation plots depending on the reagent. **d** Secondary structure analysis of HT according to the specific reagents used. **e** Stress-relaxation curves. Compression rate: 10%/min. Constant strain: 50%. Stress relaxation time: 500 s. Inset: compressive tests. **f** Stiffness–energy dissipation plots depending on the reagent.

that pigmentation and mineralization are responsible for the high stiffness and properties of HTs for mitigating shell closure forces.

Discussion

This study elucidated the structure–property relationship of the inner periostracum, highlighting its role as a graded material functionalized with different applied stresses on both sides. Due to this adaptation, the inner periostracum is well suited for linking biological tissue and inorganic material. Strain-dependent FT-IR analysis further increases our knowledge on the structure-property relationship (see Fig. 6a). At the tissue end, the FT-IR results revealed that the intensity of the 1515 cm^{-1} peak for Tyr (mainly an IDR reporter) decreased during tension. These findings suggest that packed IDRs are stretched and thinned during extension, akin to previous observation for silk resilin[23]. Additionally, the 1657 cm^{-1} peak corresponding to the random coil slightly increased, indicating that a few regions of β-strands transformed into random coils due to the slippage of β-strands during tension. This finding aligns with the molecular mechanism that is associated with energy dissipation induced by the slip motion of β-strands in β-sheet-rich silks[32] (see Fig. 6b). On this side, bound water molecules play a role in increasing the movement of β-strands through weakened hydrogen bonding. At the shell end, the intensity of the amide I peak at 1632 cm^{-1} decreased at 20% strain, whereas it increased above 20% strain (see Fig. 6a). This result indicated that the open pores closed at 20% strain, while the protein network began to compress above 20% strain. Thus, the intermediate water filled in the channel was forced out as a damping mechanism (see Fig. 6b).

Water plays a crucial role in the mechanical properties of biological materials[20,21]. The importance of the water interaction strength within protein materials has been described in a previous study as follows: water-ion > water–water = water-polar group > water-hydrophobic Group[33].

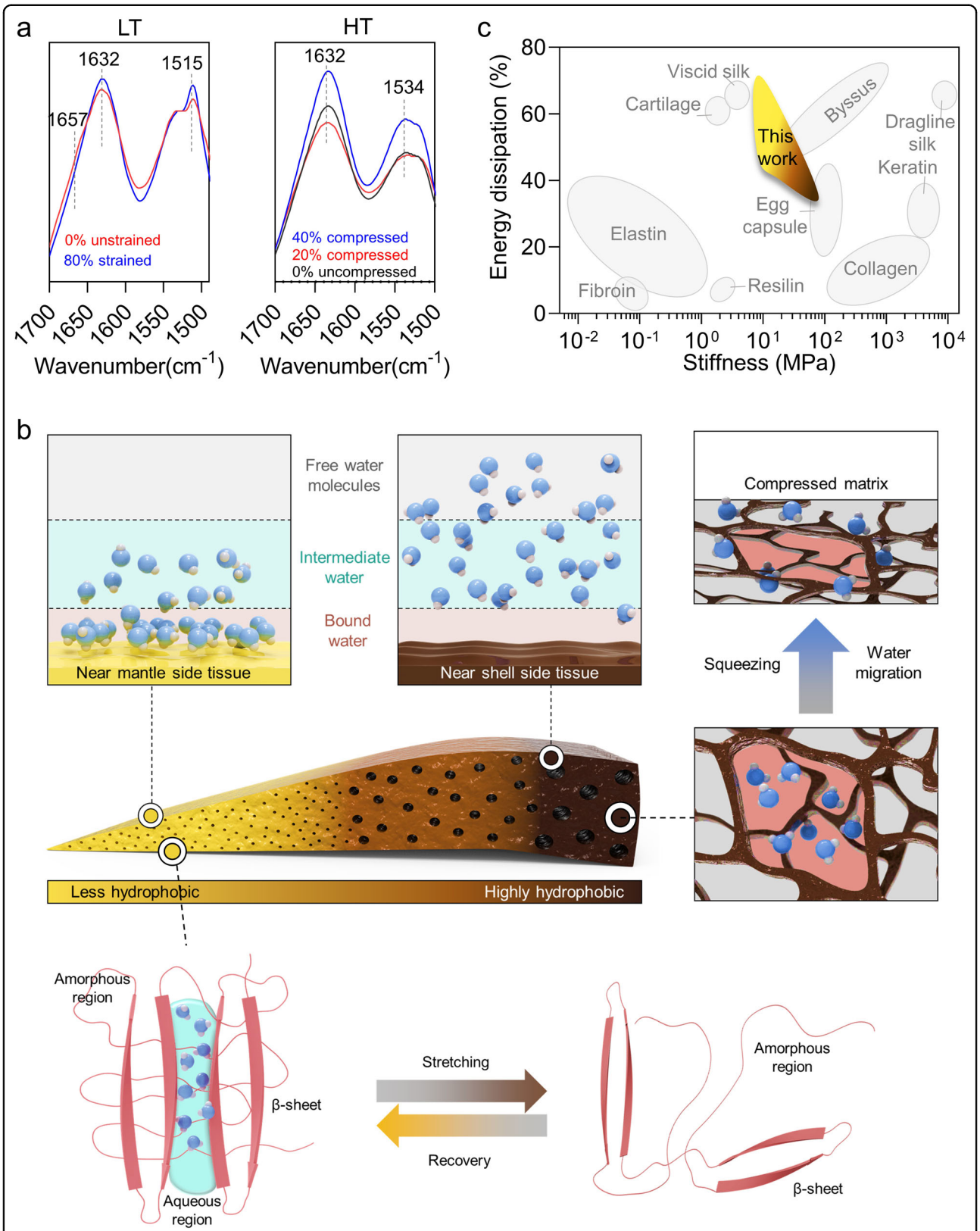

Fig. 6 Model for energy dissipation in the graded inner periostracum. a FT-IR spectra depending on the mechanical loading. Left: LTs with different tensile strains. Right: HT with different compressive strains. **b** Schematic illustration of the energy dissipation on both sides. **c** Comparison of the mechanical properties of the inner periosteum with those of other biomaterials[22,32,39–46] (Table S4).

In the inner periostracum, water assumes different roles depending on the pigment levels (see Fig. 6b). As periostracin proteins are water-absorbent building blocks, water molecules can interact with proteins on the nonpigmented side near the tissue. Polar groups such as Gly and Tyr are likely to interact with water molecules to prevent expulsion from the protein matrix when the β-sheet chains are extended. Conversely, hydrophobic pigments inhibit water molecules from binding to proteins; as a result, intermediate water molecules are stored in open pores at the shell side of the periostracum. When subjected to compressive stress, water molecules can be squeezed out due to the weak interaction between water and pigments.

This study demonstrated that the dual operation of a stress-absorbable system contributes to the long-term stability of the inner periostracum. As the barrier between the EPS and seawater, the inner periostracum exhibits high durability, ensuring that the EPS environment is protected against dissolution by seawater. Despite variable pH levels and salt concentrations in seawater, macromolecules (such as proteins and carbohydrates) involved in the biomineralization of prismatic and nacreous layers are enclosed and concentrated in the EPS[9]. Furthermore, the removal of macromolecules from EPSs has been shown to reduce the growth rate of shells[34]. Therefore, the mechanical durability of the inner periostracum is critical for the physiological functions that support mussel growth.

The energy dissipation ability of the periostracum is comparable to that of high-energy dissipative materials, such as silk, byssus, and marine egg capsules (see Fig. 6c). The shock-absorbing capability of these materials has been elucidated in protein elastomer systems[35,36]. Specifically, this difference has been attributed to the molecular properties of the constituent proteins in elastomers. For instance, in α-helix-rich protein elastomers, such as marine egg capsules, a transition from an α-helix to a β-sheet occurs during extension[37]; in contrast, β-sheet-rich protein fibers, such as spider silk, exhibit slip motion of β-strands[38]. In this study, the periostracum exhibited dual modes for absorbing different stresses. With their unique molecular and structural characteristics (e.g., hydrophobicity and secondary structures), periostracin proteins offer a potent alternative and have the potential to inspire the design of next-generation hydrogels. Furthermore, this research provides new opportunities for hierarchical structure fabrication in the fields of biointerfaces and tissue engineering, enabling the development of complex materials with energy absorption capabilities and stiffness gradients.

Experimental procedures

Preparation of the inner periostracum

The inner periostraca of the mussels was harvested using a surgical blade and subsequently stored at −80 °C until the experiments were performed. Before use, the plants were immediately cut into three parts that were clearly classified according to their pigmentation. All the samples were lyophilized and weighed.

Electron microscopy

The samples were flash-frozen under liquid nitrogen and cut into cross-sections for SEM (JSM-6010LV, JEOL, Japan). The tissues were coated with gold and transferred to a sample mount. The regions of interest were observed at 10 kV. For TEM (JEM1011, JEOL, Japan), the samples were embedded in epoxy resin. Before the embedding step, the samples were fixed for 4 h in 3% glutaraldehyde and 1.5% paraformaldehyde in 0.1 M cacodylate buffer (pH 7). Further fixation was performed in 1% OsO_4 for 2 h. The fixed samples were serially dehydrated using ethanol (50%, 70%, 80%, and 90%) for 30 min and incubated with 100% ethanol overnight. The buffer transition was performed in propylene oxide solution for 1 h, and this process was repeated twice. The sample was subsequently infiltrated with a resin solution under vacuum. The samples were finally polymerized in resin at 80 °C. The embedded samples were sectioned to a thickness of 100 nm by an ultramicrotome. Thin blocks were mounted on carbon-coated copper grids for imaging.

Amino acid analysis

Lyophilized samples weighing 4–6 mg were hydrolyzed in 200 µl of 6 M HCl containing 5% saturated phenol in a sealed vial for 24 h at 110 °C. Thereafter, the hydrolysates were flash evaporated using a vacuum evaporator at 60 °C and washed twice with water and methanol. The dried samples were resuspended in 0.1 M HCl. The soluble fractions were subjected to an amino acid analyzer (ninhydrin-based SYKAM System S4300; SYKAM, Germany). All tests were repeated as $n = 3$ independent samples.

Quantification of insoluble pigments

The insoluble black pigment content was measured using a UV–Vis spectrometer (Optizen, Korea). The pigments from the periostracum were solubilized by alkaline peroxidation (5% of 30% hydrogen peroxide and 2.5% of 10 N NaOH). Serial standard curves (0.01, 0.025, 0.05, and 0.1 mg/ml) of the solubilized pigments were obtained using a UV–Vis spectrometer (Fig. S6). To determine the amount of pigment, the absorbance at 300 nm of the soluble pigment solution of each cutout was obtained after alkaline peroxidation. It is generally established that alkaline peroxide labile pigments arise from quinone-mediated covalent crosslinking. All tests were repeated with $n = 3$ independent samples.

Inductively coupled plasma-atomic emission spectroscopy (ICP–AES)

Acid hydrolysis of the samples was performed in 6 M HCl and 5% phenol. The soluble fractions obtained from acid hydrolysis were added to 30% hydrogen peroxide, and the inorganic components (Ca, Mg, P, and Fe) were detected using ICP–AES (iCAP6500DUO, Thermo Scientific, Waltham, MA). All tests were repeated with $n = 3$ independent samples.

Phenylboronate chromatography

The periostracum was hydrolyzed in 6 M HCl and 5% phenol solution at 110 °C for 24 h. The soluble hydrolysate was subjected to phenylboronate chromatography to capture catecholic crosslinks. An Affi-gel boronate column (1536103, Bio-Rad, Hercules, CA) was equilibrated with 0.1 M sodium phosphate buffer (pH 7.45), and soluble hydrolysate in the binding buffer was added to the column. A 2.5 mM ammonium bicarbonate solution was used to desalt the column. The binding chemicals were eluted with 5% acetic acid.

Tryptic digestion

The periostracum was finely ground under liquid nitrogen. The samples were immersed in 6 M urea and 0.4 M ammonium bicarbonate solution to denature the protein structures. Tris(2-carboxyethyl)phosphine (TCEP) was added to the solution to a concentration of 5 mM, and the mixture was incubated for 60 min while shaking. Iodoacetamide was also added to a 25 mM solution, and the mixture was incubated for 60 min in the dark. The solution was diluted 10 times using a 40 mM ammonium bicarbonate solution. Finally, crude peptides were obtained by trypsin digestion for 16 h at 37 °C. The samples were subsequently subjected to liquid chromatography coupled with tandem mass spectrometry (LC–MS/MS).

Mass spectrometry

To identify the constituent proteins, nano-LC–MS/MS analysis was performed with an Easy n-LC (Thermo Fisher, San Jose, CA) and an LTQ Orbitrap XL mass spectrometer (Thermo Fisher, San Jose, CA) equipped with a nanoelectrospray source. The peptides extracted by in-solution tryptic digestion were separated on a C18 nanopore column (150 mm × 0.1 mm, 3 μm pore size; Agilent). The mobile phase A for LC separation was 0.1% formic acid and 3% acetonitrile in deionized water, and the mobile phase B was 0.1% formic acid in acetonitrile. The chromatography gradient was designed for a linear increase from 0% B to 40% B in 40 min, 40% B to 60% B in 4 min, 95% B in 4 min, and 100% A in 6 min. The flow rate was maintained at 1500 nL/min. Mass spectra were acquired using data-dependent acquisition with a full mass scan (350–1200 m/z) followed by 10 MS/MS scans. For MS1 full scans, the Orbitrap resolution was 15,000, and the automatic gain control (AGC) was 2×10^5. For MS/MS at the LTQ, the AGC was 1×10^4. To identify the constituent proteins, the acquired spectra were compared with the transcriptome using PEAKS software.

To identify the catecholic compounds in the periostracum, the eluted sample solution obtained by phenylboronate chromatography was subjected to liquid chromatography (Ultimate3000, Thermo Scientific, Waltham, MA) and ESI-MS/MS (Velos Pro, Thermo Scientific, Waltham, MA). The compounds were separated using a C18 column (50 mm × 2.1 mm, 5 μm pore size; Thermo Scientific) with the same gradient. Mass spectra were acquired with a full mass scan (100–2000 m/z) followed by MS/MS scans at 40 kV.

FT-IR analysis

FT-IR spectra were acquired using an Alpha II instrument (Bruker, Billerica, MA) in attenuated total reflection (ATR) mode. Measurements were performed with a nominal resolution of 4 cm^{-1} and 48 scans and a frequency range of 400–4000 cm^{-1}. All the samples were vigorously washed with water after reagent treatment immediately before testing. According to previous Studies[22,23], we obtained the secondary structures of the samples through qualitative analysis. The secondary structures, including β-sheets and random coils, were assigned to the amide I and II bands as follows: β-sheets (approximately 1630 cm^{-1} in amide I and approximately 1530 cm^{-1} in amide II) and random coils (approximately 1660 cm^{-1}). In addition, the assignments of large side chains, such as Tyr to 1617 cm^{-1} in amide I and 1515 cm^{-1} in amide II, corresponded well with those of other proteins and peptides. All the spectra presented in the figures were corrected by baseline subtraction.

Mechanical tests

Periostracum specimens (0.8–1 mm wide, 1–2 mm long, 0.15–0.6 mm thick) were carefully cut using a surgical blade for tensile testing (TA1, AMETEK, Berwyn, PA). All tests were repeated with $n = 5$ independent samples. Hydrated samples were prepared by submerging in artificial seawater for at least 3 h. These samples were removed from the water immediately before the experiment. Dried samples were prepared by evaporating water at 22 °C and 30% RH for 24 h. Both sides of the samples were attached to pads to inhibit sliding, and the length from pad to pad was fixed at 10 mm. Tensile tests were performed at a rate of 5 mm/min. Cyclic tensile tests were also conducted at the same tension rate. The samples were rehydrated in seawater for 5 min after every three cycles.

For compression and stress relaxation tests, samples (0.8–1.4 mm wide, 1 mm long, 0.15–0.5 mm thick) were carefully prepared in DI water. Cyclic compression tests were conducted using the instrument in a chamber filled with artificial seawater at a compression rate of 10%/min. The change in force was monitored at 50% constant strain for 500 s to measure the relaxed stress. The relaxed stress was calculated as the difference between the maximum stress at 0 s and the stress at 500 s.

To investigate the relationships between the mechanical and biomolecular properties, the periostracum samples were chemically modified using several reagents. DOPA crosslinking was achieved in 100 mM $NaIO_4$ solution for 3 h. For crosslinking of tyrosine residues in disordered regions, the samples were irradiated by UV light in 1 mM Ru(II)bpy and 10 mM APS solution for 3 h. Demineralization was performed in 0.5 M EDTA solution for 3 h. Depigmentation was performed by alkaline peroxidation with heat application at 70 °C for 30 min. The peroxidation solution was prepared by mixing 5% 3% H_2O_2 solution and 2.5% 10 N NaOH. For β-sheet removal, the samples were incubated in 6 M urea dissolved in water for 3 h.

ToF-SIMS

Molecular distributions of the major amino acids, including Gly and Tyr, were visually observed using a ToF-SIMS 5 instrument (ION-TOF, Münster, Germany) with a pulsed 30 keV Bi_3^+ primary ion beam in the spectrometry mode for positive ions. The Bi_3^+ currents were 0.5 pA and measured using a Faraday cup before acquiring the data. Internal mass calibration was performed for all ToF-SIMS spectra using the peaks corresponding to CH_3^+, $C_2H_3^+$, $C_3H_5^+$, and $C_4H_7^+$ in positive ion mode before further analysis. Low-energy electrons were supplied onto the surface of the specimen using an electron flood gun for charging compensation during analysis. The inner periostracum was embedded into the epoxy block. The block was cut to a size of 100 nm and placed on glass. Finally, ToF-SIMS images ($300 \times 300\ \mu m^2$, 256×256 pixels) of the fragmented masses of Tyr were captured.

Acknowledgements

We acknowledge Prof. J. Herbert Waite (UCSB) for helpful discussions and comments on the manuscript. This work was supported by the National Research Foundation of Korea (NRF) grant funded by the Korean government (MSIT) (No. 2019M3C1B7025093), the National Research Foundation of Korea (NRF) grant funded by the Korean government (MSIT) (No. 2022R1A2C2007874), and the Technology Innovation Program (20009508, Development of Biodegradation Evaluation Technology for Building Circular Ecosystem Related to Bioplastic Industry) funded by the Ministry of Trade, Industry & Energy (MOTIE, Korea). This research was also supported by a grant from the Korean Health Technology R&D Project through the Korea Health Industry Development Institute (KHIDI), funded by the Ministry of Health & Welfare Republic of Korea (grant number: HP23C0190000023). This research was also supported by the KRICT Core Project (SS2242-10). This study was carried out with the support of R&D Program for Forest Science Technology (Project No. 2023499B31-2425-AA02) provided by Korea Forest Service (Korea Forestry Promotion Institute).

Author details

[1]Division of Environmental Science and Engineering, Pohang University of Science and Technology (POSTECH), Pohang 37673, Republic of Korea. [2]School of Interdisciplinary Bioscience and Bioengineering, Pohang University of Science and Technology (POSTECH), Pohang 37673, Republic of Korea. [3]Center for Scientific Instrumentation, Korea Basic Science Institute (KBSI), Cheongju, Chungcheongbuk-do 28119, Republic of Korea. [4]Department of Energy Chemical Engineering, Kyungpook National University, 2559, Gyeongsang-daero, Sangju, Gyeongsangbuk-do 37224, Republic of Korea. [5]Department of Organic Materials Engineering, Chungnam National University, Daejeon 34134, Republic of Korea. [6]School of Energy and Chemical Engineering, Ulsan National Institute of Science and Technology (UNIST), Ulsan 44919, Republic of Korea. [7]Research Center for Bio-based Chemistry, Korea Research Institute of Chemical Technology (KRICT), Ulsan 44429, Republic of Korea. [8]Department of Polymer Science and Engineering and Program in Environmental and Polymer Engineering, Inha University, Incheon 22212, Republic of Korea. [9]Institute for Convergence Research and Education in Advanced Technology, Yonsei University International Campus I-CREATE, Incheon 21983, Republic of Korea

Author contributions

H.K., H.L., S.K., and C.L. performed the experiments. J.M.K. and H.Kw. analyzed the data. H.K., D.X.O., and D.S.H. wrote the manuscript with input from all the coauthors. D.X.O. and D.S.H. supervised the project.

Conflict of interest

D.S.H. and H.K. filed a patent application related to this work (patent applicant: Pohang University of Science and Technology; Inventors: Dong Soo Hwang & Hyungbin Kim; Application number: KR 10-2023-0085929; Status: submitted.

Supplementary information The online version contains supplementary material available at https://doi.org/10.1038/s41427-024-00543-x.

Received: 13 October 2023 Revised: 24 January 2024 Accepted: 1 February 2024.
Published online: 26 April 2024

References

1. Yoo, H. Y. et al. Sugary interfaces mitigate contact damage where stiff meets soft. *Nat. Commun.* **7**, 11923 (2016).
2. Boys, A. J. et al. Understanding the stiff-to-compliant transition of the meniscal attachments by spatial correlation of composition, structure, and mechanics. *A. C. S. Appl. Mater. Interfaces* **11**, 26559–26570 (2019).
3. Waite, J. H., Vaccaro, E., Sun, C. & Lucas, J. M. Elastomeric gradients: A hedge against stress concentration in marine holdfasts? *Philos. Trans. R. Soc. Lond. B Biol. Sci.* **357**, 143–153 (2002).
4. Kamat, S., Su, X., Ballarini, R. & Heuer, A. H. Structural basis for the fracture toughness of the shell of the conch Strombus gigas. *Nature* **405**, 1036–1040 (2000).
5. Bubel, A. An electron-microscope study of periostracum formation in some marine bivalves. II. The cells lining the periostracal groove. *Mar. Biol.* **20**, 222–234 (1973).
6. Kang, J.-Y. Chemical defence in mussels: Antifouling effects of the periostracum on algal spore settlement in the mussel *Mytilus edulis*. *Fish. Aquat. Sci.* **19**, 7 (2016).
7. Wählisch, F. C. et al. Surviving the surf: The tribomechanical properties of the periostracum of Mytilus sp. *Acta Biomater.* **10**, 3978–3985 (2014).
8. Taylor, J. D. & Kennedy, W. J. The influence of the periostracum on the shell structure of bivalve molluscs. *Calcif. Tissue Res.* **3**, 274–283 (1969).
9. Crenshaw, M. A. The inorganic composition of molluscan extrapallial fluid. *Biol. Bull.* **143**, 506–512 (1972).

10. Miserez, A., Schneberk, T., Sun, C., Zok, F. W. & Waite, J. H. The transition from stiff to compliant materials in squid beaks. *Science* **319**, 1816–1819 (2008).
11. Claussen, D. L., Gerald, G. W., Kotcher, J. E. & Miskell, C. A. Pinching forces in crayfish and fiddler crabs, and comparisons with the closing forces of other animals. *J. Comp. Physiol. B* **178**, 333–342 (2008).
12. Nam, S., Hu, K. H., Butte, M. J. & Chaudhuri, O. Strain-enhanced stress relaxation impacts nonlinear elasticity in collagen gels. *Proc. Natl Acad. Sci. USA* **113**, 5492–5497 (2016).
13. Huang, J. et al. Ultrahigh energy-dissipation elastomers by precisely tailoring the relaxation of confined polymer fluids. *Nat. Commun.* **12**, 3610 (2021).
14. Waite, J. H., Saleuddin, A. S. M. & Andersen, S. O. Periostracin—A soluble precursor of sclerotized periostracum inMytilus edulis L. *J. Comp. Physiol. B* **130**, 301–307 (1979).
15. Kawecki, M. & Bernard, L. Database of proteinogenic amino acid reference spectra for bismuth-cluster ToF-SIMS. II. Positive polarity. *Surf. Sci. Spectra* **25**, 015002 (2018).
16. Weiner, S. Mollusk shell formation: Isolation of two organic matrix proteins associated with calcite deposition in the bivalve Mytilus californianus. *Biochemistry* **22**, 4139–4145 (1983).
17. Lee, M. et al. Network of cyano-p-aramid nanofibres creates ultrastiff and water-rich hydrospongels. *Nat. Mater.* **23**, 414–423 (2024).
18. Miserez, A., Rubin, D. & Waite, J. H. Cross-linking chemistry of squid beak. *J. Biol. Chem.* **285**, 38115–38124 (2010).
19. Ozeki, H., Ito, S., Wakamatsu, K. & Ishiguro, I. Chemical characterization of pheomelanogenesis starting from dihydroxyphenylalanine or tyrosine and cysteine. Effects of tyrosinase and cysteine concentrations and reaction time. *Biochim. Biophys. Acta* **1336**, 539–548 (1997).
20. Huang, W. et al. How water can affect keratin: Hydration-driven recovery of bighorn sheep (Ovis canadensis) horns. *Adv. Funct. Mater.* **29**, 1901077 (2019).
21. Quan, H., Kisailus, D. & Meyers, M. A. Hydration-induced reversible deformation of biological materials. *Nat. Rev. Mater.* **6**, 264–283 (2021).
22. Mu, X., Yuen, J. S. K. Jr, Choi, J. & Kaplan, D. L. Conformation-driven strategy for resilient and functional protein materials. *Proc. Natl Acad. Sci. USA* **119**, e2115523119 (2022).
23. Qin, G., Hu, X., Cebe, P. & Kaplan, D. L. Mechanism of resilin elasticity. *Nat. Commun.* **3**, 1003 (2012).
24. Barth, A. The infrared absorption of amino acid side chains. *Prog. Biophys. Mol. Biol.* **74**, 141–173 (2000).
25. Murayama, K. & Tomida, M. Heat-induced secondary structure and conformation change of bovine serum albumin investigated by fourier transform infrared spectroscopy. *Biochemistry* **43**, 11526–11532 (2004).
26. Hu, X., Kaplan, D. & Cebe, P. Dynamic protein-Water relationships during beta-sheet formation. *Macromolecules* **41**, 3939–3948 (2008).
27. Harrington, M. J., Masic, A., Holten-Andersen, N., Waite, J. H. & Fratzl, P. Iron-clad fibers: A metal-based biological strategy for hard flexible coatings. *Science* **328**, 216–220 (2010).
28. Zeng, H., Hwang, D. S., Israelachvili, J. N. & Waite, J. H. Strong reversible Fe3+-mediated bridging between dopa-containing protein films in water. *Proc. Natl Acad. Sci. USA* **107**, 12850–12853 (2010).
29. Weaver, J. C. et al. The stomatopod dactyl club: A formidable damage-tolerant biological hammer. *Science* **336**, 1275–1280 (2012).
30. Vaccaro, E. & Waite, J. H. Yield and post-yield behavior of mussel byssal thread: A self-healing biomolecular material. *Biomacromolecules* **2**, 906–911 (2001).
31. Zhang, X. et al. Extensible and self-recoverable proteinaceous materials derived from scallop byssal thread. *Nat. Commun.* **13**, 2731 (2022).
32. Xu, Z. & Buehler, M. J. Mechanical energy transfer and dissipation in fibrous beta-sheet-rich proteins. *Phys. Rev. E Stat. Nonlin. Soft Matter Phys.* **81**, 061910 (2010).
33. Dargaville, B. L. & Hutmacher, D. W. Water as the often neglected medium at the interface between materials and biology. *Nat. Commun.* **13**, 4222 (2022).
34. Xie, J. et al. Influence of the extrapallial fluid of Pinctada fucata on the crystallization of calcium carbonate and shell Biomineralization. *Cryst. Growth Des.* **16**, 672–680 (2016).
35. Gosline, J. et al. Elastic proteins: Biological roles and mechanical properties. *Philos. Trans. R. Soc. Lond. B Biol. Sci.* **357**, 121–132 (2002).
36. Rapoport, H. S. & Shadwick, R. E. Mechanical characterization of an unusual elastic biomaterial from the egg capsules of marine snails (Busycon spp.). *Biomacromolecules* **3**, 42–50 (2002).
37. Miserez, A., Wasko, S. S., Carpenter, C. F. & Waite, J. H. Non-entropic and reversible long-range deformation of an encapsulating bioelastomer. *Nat. Mater.* **8**, 910–916 (2009).
38. Keten, S., Xu, Z., Ihle, B. & Buehler, M. J. Nanoconfinement controls stiffness, strength and mechanical toughness of beta-sheet crystals in silk. *Nat. Mater.* **9**, 359–367 (2010).
39. Gosline, J. M., Guerette, P. A., Ortlepp, C. S. & Savage, K. N. The mechanical design of spider silks: from fibroin sequence to mechanical function. *J. Exp. Biol.* **202**, 3295–3303 (1999).
40. Bursać, P. M., Obitz, T. W., Eisenberg, S. R. & Stamenović, D. Confined and unconfined stress relaxation of cartilage: Appropriateness of a transversely isotropic analysis. *J. Biomech.* **32**, 1125–1130 (1999).
41. Weizel, A. et al. Complex mechanical behavior of human articular cartilage and hydrogels for cartilage repair. *Acta Biomater.* **118**, 113–128 (2020).
42. Boettcher, K. et al. The structure and mechanical properties of articular cartilage are highly resilient towards transient dehydration. *Acta Biomater.* **29**, 180–187 (2016).
43. Rapoport, H. S. & Shadwick, R. E. Reversibly labile, sclerotization-induced elastic properties in a keratin analog from marine snails: Whelk egg capsule biopolymer (WECB). *J. Exp. Biol.* **210**, 12–26 (2007).
44. Annabi, N. et al. Engineered cell-laden human protein-based elastomer. *Biomaterials* **34**, 5496–5505 (2013).
45. Bellingham, C. M. et al. Recombinant human elastin polypeptides self-assemble into biomaterials with elastin-like properties. *Biopolymers* **70**, 445–455 (2003).
46. Liu, J. et al. Energy dissipation in mammalian collagen fibrils: Cyclic strain-induced damping, toughening, and strengthening. *Acta Biomater.* **80**, 217–227 (2018).